

Article

Age and Origin of the Mesoproterozoic Iron Oxide-Apatite Mineralization, Cheever Mine, Eastern Adirondacks, NY

Jeffrey R. Chiarenzelli ^{1,*}, Marian V. Lupulescu ², Sean P. Regan ³ and Jared W. Singer ⁴

¹ Department of Geology, St. Lawrence University, Canton, NY 13617, USA

² New York State Museum, Research and Collections, Albany, NY 12230, USA; Marian.Lupulescu@nysed.gov

³ Department of Geosciences, University of Alaska Fairbanks, 900 Yukon Drive, Fairbanks, AK 99775, USA; sregan5@alaska.edu

⁴ Department of Earth and Environmental Sciences, Rensselaer Polytechnic Institute, Troy, NY 12180, USA; jared.wesley.singer@gmail.com

* Correspondence: jchiaren@stlawu.edu

Received: 2 July 2018; Accepted: 7 September 2018; Published: 12 September 2018



Abstract: At the Cheever Mine, located in the eastern Adirondack Mountains of the Mesoproterozoic Grenville Province, iron oxide-apatite ore forms a narrow (<3 m) sheet cross-cutting metasomatically altered, magnetite-bearing, albite-rich leucogranitic host rocks of the Lyon Mountain Granite suite. Zircon from the ore and five samples of country rock were dated by Laser Ablation-Multi-Collector-Inductively Coupled Plasma-Mass Spectrometry. The ore yielded a Concordia age of 1033.6 ± 2.9 Ma while three samples of host rock yielded ages of 1036.3 ± 2.9 , 1040 ± 11 , and 1043.9 ± 4.1 Ma. Two additional samples of host rock yielded older ages of 1059.6 ± 3.4 and 1066.0 ± 6.3 Ma and contain zircon xenocrystic cores with $^{207}\text{Pb}/^{206}\text{Pb}$ ages up to 1242 Ma. The zircons analyzed, including those separated from the ore, have characteristics typically associated with an igneous origin including size, shape, inclusions, oscillatory zoning, typical chondrite-normalized REE patterns, U contents, and U/Th ratios. This data establishes the age of the ore and alteration and a temporal, and likely genetic, connection between the ore and members of the Lyon Mountain Granite suite. A model invoking melting of Shawinigan country rocks, magmatic differentiation, and long-lived magmatic and metasomatic input along extensional fault conduits is proposed for the ore's genesis. At the Cheever Mine, magmatic hydrothermal fluids and/or post-intrusion alteration appears not to have had a major impact on zircon, which preserves original U-Pb systematics.

Keywords: iron oxide-apatite deposits (IOA deposits); U-Pb zircon geochronology; Adirondack Mountains; Grenville Province; Lyon Mountain Granite; Cheever Mine

1. Introduction

Iron oxide-apatite (IOA) deposits have served as an important source of iron in northern New York from the early 1800s to recent times [1]. The IOA ores of the Kiruna-Malmberget and Bergslagen ore provinces in Sweden to which they are often compared are the major source of iron to the European Union [2]. In addition to magnetite, martite, and/or hematite, apatite can be readily separated from many of these deposits and is found enriched in tailings from past mining operations. The use of apatite-rich tailings for fertilizer was briefly attempted [3]. However, renewed interest exists because of rare earth elements (REEs) that can occur at relatively high (ca. up to 20 wt. %) concentrations in the apatite structure [4,5]. Rare-earth deposits are known to be associated with other IOA deposits in the

Grenville such as the Kwyjibo deposit of Canada with resources of 6.92 Mt at 2.72% total rare earth oxides [6].

Numerous studies, particularly of the early Proterozoic Kiruna deposit and those of Pliocene age in El Lago in Chile and elsewhere, have led to major advances in our understanding of IOA deposits [2,7–9]. These deposits are considered a subgroup of iron oxide-alkali altered (IOAA) mineralized systems [10,11] and are related to iron-oxide copper-gold (IOCG) deposits [9–11]. The application of U-Pb zircon geochronology [12,13], isotopic studies [7,13–17], geochemistry [10,18,19], thermometry and fluid inclusions [20], new petrologic models [21], textures [22,23], and field relations [8,9,11] have led to a better understanding of the age and origin of these deposits. A magmatic and/or high-temperature hydrothermal/metasomatic fluid origin has been proposed to account for many of the features observed in IOA deposits and controversy remains concerning the dominant process [18]. In addition, the alteration of bulk-rock chemistry and isotopic systems in surrounding rocks is well-documented [10–16].

Herein, we provide new data that help constrain the age and origin of the late Mesoproterozoic IOA deposits of the eastern Adirondack Mountains in the southern Grenville Province (Figures 1 and 2). We conclude that IOA ore at Cheever Mine: (1) is of intrusive magmatic origin, (2) is spatially and temporally associated with metasomatically-altered ferroan leucogranites of the Lyon Mountain Granite suite (LMG), and (3) was emplaced along fault systems developed during the extensional phase of the Ottawa Orogeny (ca. 1040 Ma). The Cheever Mine is especially instructive as Na-metasomatism associated with IOA ores throughout the area [15,18], appears to have little or no impact on the zircon in the host and ore samples studied.

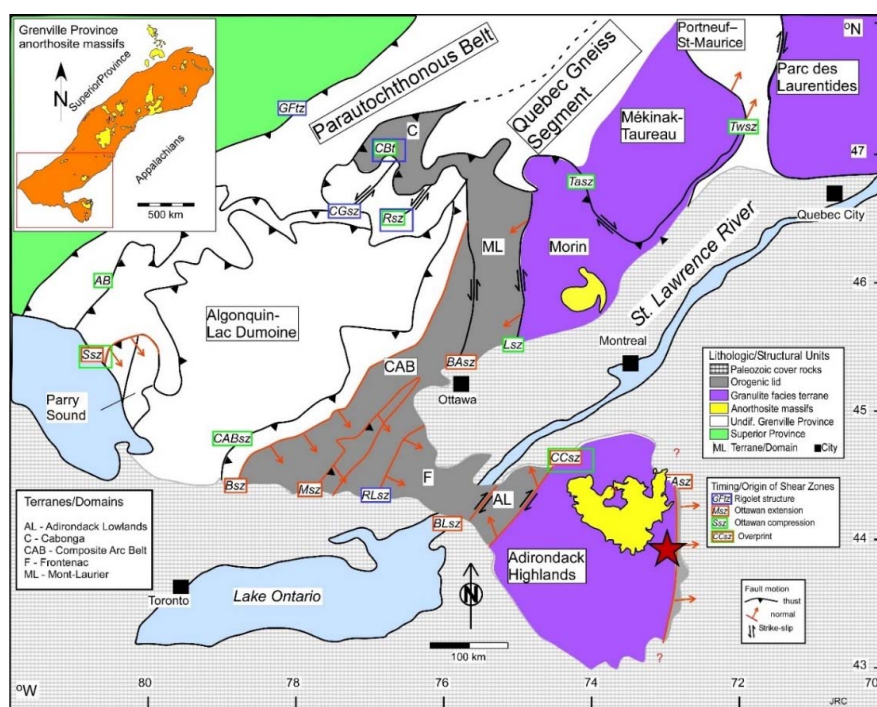


Figure 1. Generalized geologic and tectonic map of the southern Grenville Province (modified from Rivers, T. Can. J. of Earth Sci. 2012 [24]). Black and red lines show major terrain/domain/structural boundaries. Major shear zones are shown by age, tectonic affiliation, and movement history. Shear zones include: Abt: Allochthon boundary thrust, BsZ: Bancroft, BASz: Baskatong, BLSz: Black Lake, CABsz: Composite Arc Boundary, CBT: Cabonga thrust, CCSz: Carthage-Colton, CGsz: Cagecrib, EAsz: Eastern Adirondack, GFtz: Grenville Front tectonic zone, Lsz: Labelle, Msz: Mooroton, RLSz: Robertson Lake, Rsz: Renzy, Ssz: Shawanaga, Tasz: Taureau, and Twsz: Tawachiche. Inset shows location of Figure 2 (red box), the southern Grenville Province (orange), and major anorthosite massifs (yellow).

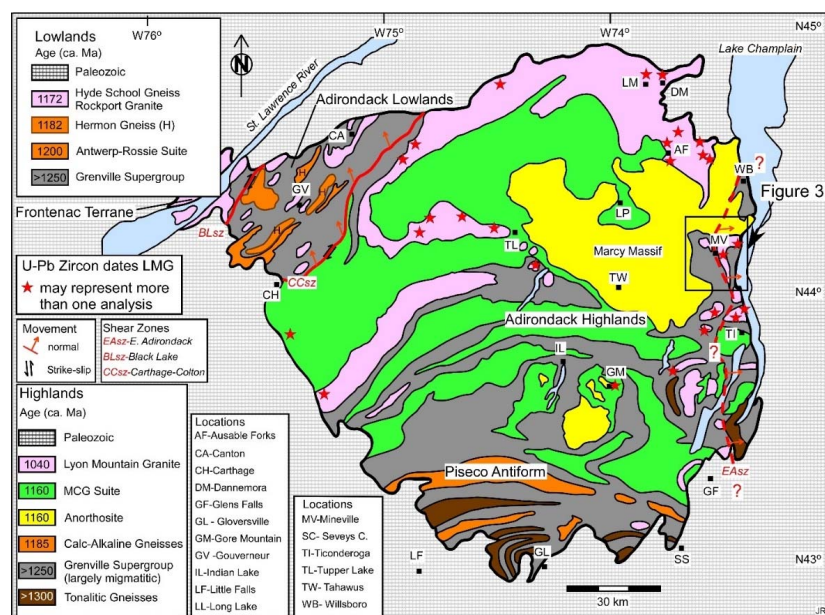


Figure 2. A generalized geological map of the Adirondack region. Colored units consist of igneous rocks dated by U-Pb zircon geochronology with ages indicated in the legend. The grey unit is metasedimentary rocks of the Grenville Supergroup deposited between 1250–1300 Ma. Separate legends are given for the Highlands and Lowlands terranes. Small red stars note sampling locations for U-Pb zircon analyses of the Lyon Mountain Granite (LMG) suite.

2. Geological Setting

The Adirondacks are a small but intensely studied portion of the Mesoproterozoic Grenville Province. Located between the Archean Superior Province and the Paleozoic rocks of the foreland of the Appalachian Orogen (Figure 1), the Grenville Province records Mesoproterozoic reworking of, and accretion to, the Laurentian margin and the eventual formation of the Supercontinent Rodinia. The Grenville Province is unique due to the large amount of massif anorthosite and related rocks (Anorthosite-Mangerite-Charnockite-Granite—AMCG suite), which are relatively rare elsewhere. These rocks are abundant in the Adirondack Highlands and make up about 65% of the exposed bedrock and were intruded near the end of the Shawinigan Orogeny (ca. 1140–1165 Ma). They are part of a protracted ferroan magmatic event of Proterozoic age, which spanned much of southeastern Laurentia [25].

The Adirondack Mountains occur as an elongate NNE-trending dome (Figure 2) whose dimensions are ca. 190 km × 140 km. Uplift began approximately 180 million years ago [26] coincident with the opening of the Atlantic Ocean. During the uplift, the overlying lower Paleozoic rocks were eroded from the dome exposing the Precambrian basement rocks. Grenville rocks in the Adirondacks are connected to the Grenville Province of Ontario and Quebec through the Thousand Islands and underneath the Paleozoic cover rocks of the Ottawa Embayment [27].

The southern part of the Grenville Province was originally subdivided into the Central Gneiss Belt, the Central Metasedimentary Belt, and the Central Granulite Terrane [28]. Decades of field and laboratory work have led to many refinements of this original classification based largely on the differences in tectonic and metamorphic histories in various areas. Rocks in the southern Grenville Province were affected by a series of four events spanning over 250 million years, collectively known as the Grenville Orogenic Cycle [29]. These four events are named the Elzevirian (1245–1220 Ma), Shawinigan (1200–1140 Ma), and Grenvillian orogenies (1090–980 Ma) with the Grenvillian Orogeny further subdivided into the Ottawan (1090–1020 Ma) and Rigolet (1010–980 Ma) pulses [24]. These discoveries have led to a classification based on the number and intensity of deformational/metamorphic events affecting a given region (Monocyclic and Polycyclic of Rivers

et. al., 2008 [30]) and original location of the terranes with respect to Laurentia. In addition, it has been widely recognized that the Grenville Province provides a glimpse into the deep roots of a continent-continent collision and serves as an ancient example of channel flow where rocks deformed during earlier events serve as the orogenic cap or lid to subsequent tectonism [24].

The Adirondacks have been subdivided into the Adirondack Highlands (AH) and Lowlands (AL) primarily based on lithology and metamorphic grade, but the original relationship between the two domains remains somewhat enigmatic [31,32]. The boundary between them known as the Carthage-Colton shear zone (Figure 2), has had a complicated kinematic history whose culmination resulted in rapid uplift of the AH and juxtaposition with the AL during tectonic exhumation and extension at ca. 1050 Ma [32–34]. The Carthage-Colton shear zone separates rocks deformed during the Shawinigan Orogeny, which lack evidence of the Ottawa event (i.e., AL), from those that record an enigmatic “Ottawan” event at 1050 Ma (i.e., AH) including the widespread growth of metamorphic zircon rims, zircon recrystallization, and Pb-loss [35–37]. The IOA deposits of the Eastern Adirondacks (EA) are part of the AH, which are dominated by the Marcy anorthosite massif and related mangeritic, charnockitic, and granitic rocks (AMCG Suite). Granulite-facies metamorphism and the deformation of rheologically weak country rocks is seen throughout the AH associated with the Shawinigan Orogeny. The spatial variability of the Shawinigan and Ottawa events has yet to be fully resolved and is the subject of current research in the region [36,37].

The iron mining district in the EA is located east of the Marcy massif and west of Lake Champlain (Figure 3). In this area, rock types include metasedimentary lithologies typical of the Grenville Supergroup [38], anorthosite and related rocks, gabbro, leucogranitic rocks of the Lyon Mountain granite, magnetite-apatite deposits, and late pegmatites [39]. Metasomatic alteration associated with the ore is largely restricted to the LMG, which hosts the mineralization [12,13,16,40]. Granulite facies metamorphism and anatexis associated with the Shawinigan Orogeny occurs only in the older rocks (i.e., metasedimentary rocks and the AMCG suite). The magnetite-apatite deposits cross-cut all lithologies except late pegmatites and are typically associated with hydrothermally-altered LMG even though the unit is also altered where no IOA deposits exist [41,42]. The LMG is a regionally extensive unit hosting a variety of iron deposits across the eastern and northern areas of the Adirondack dome (Figure 2). It has been interpreted as a ferroan leucogranitic suite associated with extensional collapse of an elevated plateau that existed after the Ottawa Orogeny [40].

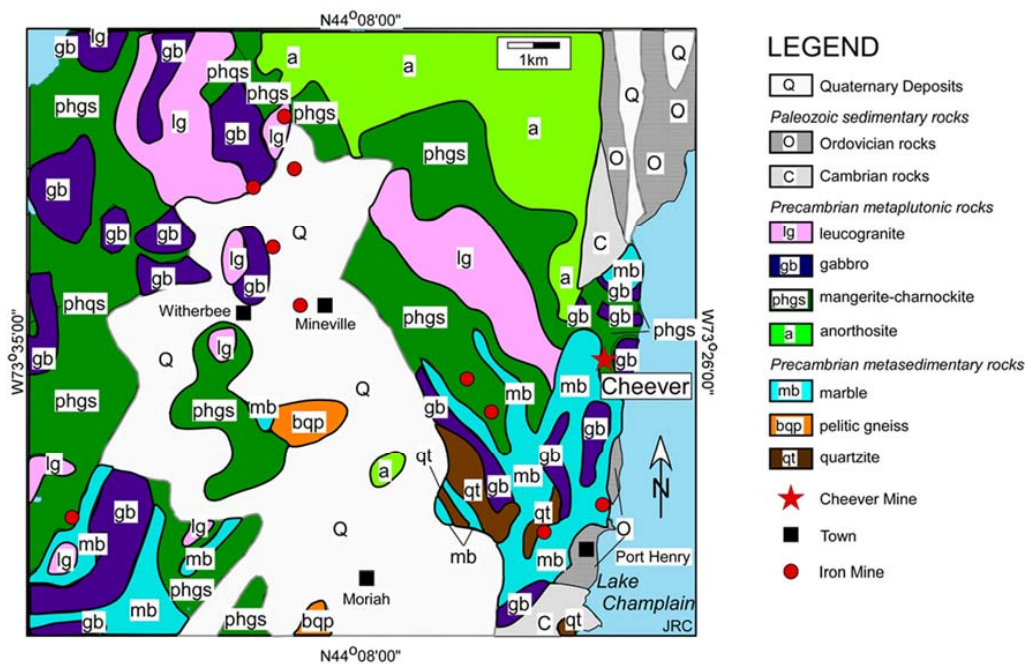


Figure 3. Map of the eastern Adirondack iron oxide-apatite (IOA) mining district.

3. Analytical Methods

The samples investigated here were collected by the authors from natural outcroppings or freshly blasted exposures along a quarry face at the Cheever Mine. A sketch map of the mine area showing sample locations and structural measurements is presented in Figure 4. Figure 5 shows key field and petrographic relations. A portion of each sample was slabbed for petrographic analysis and major element geochemistry. Corresponding samples for geochronology (1–2 kg) were processed at the Arizona Laserchron Center using standard techniques for heavy mineral separation. Once separated, the zircons were hand-picked and mounted in epoxy plugs for analysis and imaged in back-scattered electron and/or cathodoluminescence mode on a Hitachi 3400N scanning electron microscope prior to analysis. Images were used to target specific areas on each zircon grain. After analysis, a subset of zircons from each sample were selected for trace element analysis conducted at Rensselaer Polytechnic Institute by LA-ICP-MS. Major element chemistry was completed at the Peter Hooper GeoAnalytical Lab at Eastern Washington State by X-ray fluorescence. Procedures and analytical details can be found at <https://environment.wsu.edu/facilities/geoanalytical-lab/technical-notes/>. Complete analytical details are given in Appendix A.

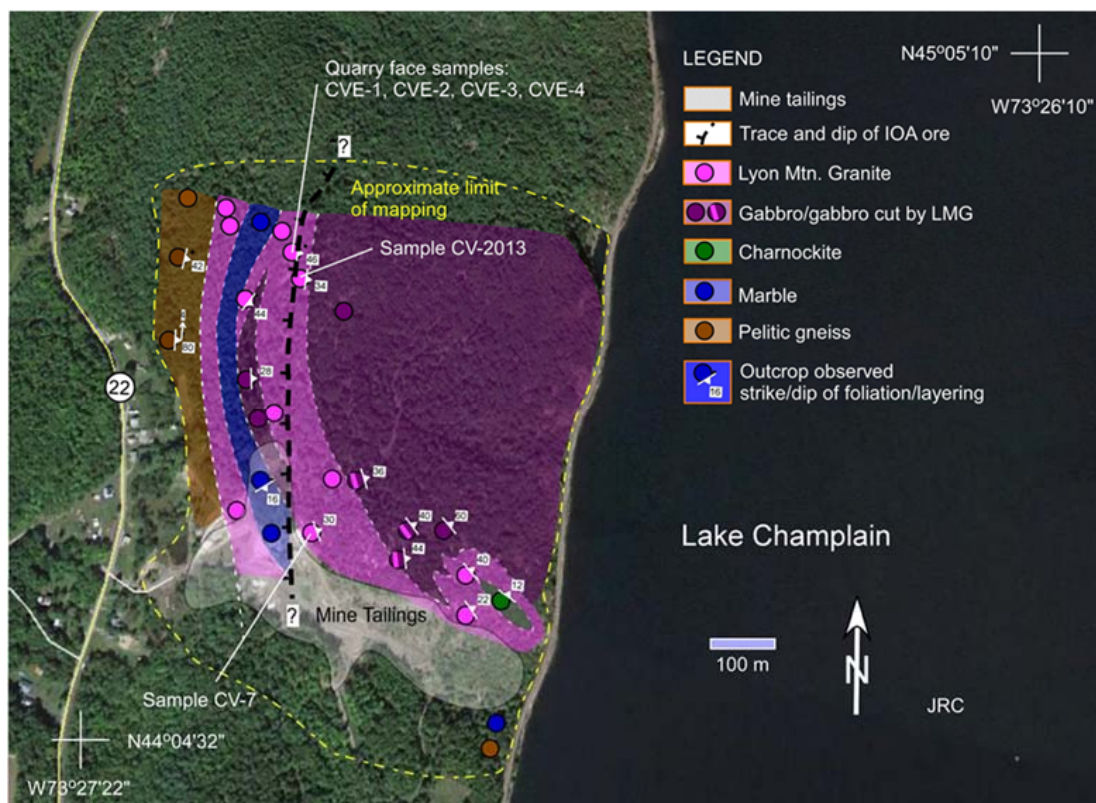


Figure 4. Geologic map of the area surrounding the Cheever Mine near Port Henry, NY. Satellite imagery from Google Earth.

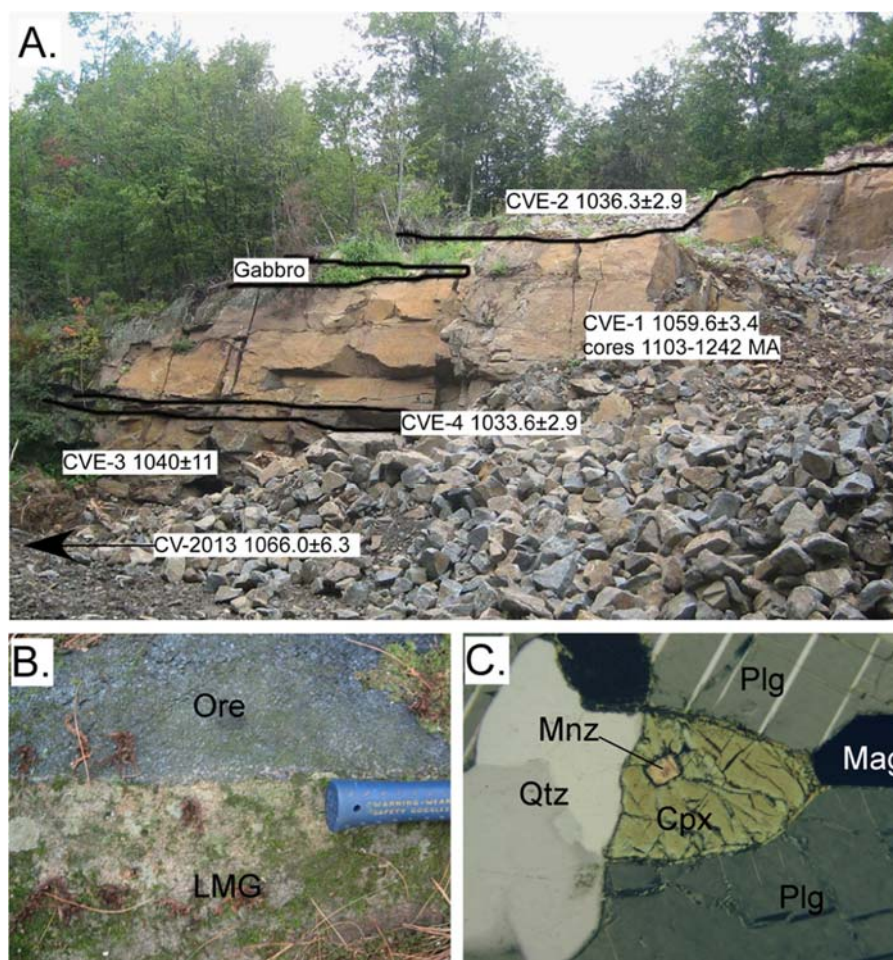


Figure 5. Typical exposure, contact relations, mineral assemblage, and compositional banding displayed at the Cheever Mine. (A) Recently developed quarry face at the Cheever Mine looking to the southwest. Ore dips away from the observer in contrast to general orientation at the site (see Figure 4). Sample numbers and results of U-Pb zircon analyses are given. (B) Sharp contact between altered leucogranite sample CV-2013 (LMG) and ore (Ore). Note fragments of pinkish country rock in the ore above the hammer handle used for scale. (C) Photomicrograph of sample CVE-3 showing petrographic relations between quartz (Qtz), plagioclase (Plg), clinopyroxene (Cpx), magnetite (Mag), and monazite (Mnz). $100\times = 2\text{ mm}$ FOV, crossed polarizers.

4. Results

Field relations. The Cheever Mine is located on a steeply sloping hillside above Lake Champlain 3.2 km north of the village of Port Henry (Figure 4). The ore strikes approximately north-south and dips moderately to the west. The exposed workings include several inclined trenches along more than 0.5 km of strike. Bedrock in the immediate area consists of rocks of the Grenville Supergroup (marble and pelitic gneiss), coronitic gabbro and derived amphibolite, pink to green granitic rocks (Figure 4), and magnetite-bearing pegmatites. A historical cross-section [43] shows the ore and host rock layers dipping and shallowing to the west. However, all the structural measurements taken in this study indicate foliation and layering in the host rocks dip to the east towards the lake, while the ore dips to the west cross-cutting the host rocks.

Three samples of host rock (CVE-1, 2, 3) and the ore (CVE-4) were taken from the hanging wall of an actively worked quarry face (Figure 5A) used for road metal or fill. Another granitic sample (CV-7) was taken from one of the numerous sheets that cross-cut and inter-finger with gabbroic rock in the footwall of the mine (Figure 4) and another was taken from a greenish granitic rock

(CV-2013) cross-cut by the ore (Figure 5B) about one hundred meters south of the quarry face depicted. The granitic host rocks sampled show variable degrees of alteration including the albitization of original feldspars, possible introduction or loss of K, Si, Al, and/or Fe, and the replacement of primary minerals by secondary phases, which is noted below. The rocks are similar in all respects to altered ferroan leucogranites associated with other iron mines in the area and share many characteristics with unaltered leucogranites of the LMG throughout the region [40]. For simplicity's sake, we will refer to them as altered leucogranites by acknowledging both their protolith and subsequent alteration.

Petrography. The five altered leucogranite samples are composed primarily of albite, quartz, and magnetite (Figure 5C). Minor amounts of clinopyroxene and mesoperthite are present in some samples. Trace phases, which were identified optically, include zircon, titanite, and monazite (Figure 5C). Late alteration phases include serpentine after clinopyroxene, hematite staining along grain boundaries, minor calcite, and minor alteration of plagioclase to clay. No evidence of deformation was noted. However, banding defined by magnetite abundance or variation in grain-size is seen in a subset of samples. The sample of ore (CVE-4) is composed predominantly of a granular, polygonal intergrowth of magnetite with minor quartz, apatite, and clinopyroxene. Monazite and zircon are trace phases while plagioclase is lacking in the ore.

Major elements. The results are shown in Table 1. The SiO₂ concentration of the host rocks ranges between 65.95% to 80.28%. The rocks are sodic with Na₂O ranging between 4.80% to 9.03% while K₂O and CaO contents are minimal. Iron oxide contents vary widely with FeO_T ranging between 1.41% to 12.21% while Al₂O₃ varies from 10.35% to 14.40%. The ore sample (CVE-4) contains 86.97% FeO_T, 4.93% SiO₂, and 2.90% P₂O₅ (all values in wt. %).

Table 1. Major element analyses by X-ray fluorescence.

Sample	SiO ₂	TiO ₂	Al ₂ O ₃	FeO _T	MnO	MgO	CaO	Na ₂ O	K ₂ O	P ₂ O ₅	LOI	TOT
CVE-1	70.59	0.39	10.99	10.68	0.01	0.05	0.36	5.77	0.64	0.05	0.00	99.52
CVE-2	80.28	0.33	10.35	1.41	0.01	0.11	0.57	4.80	1.40	0.01	0.23	99.27
CVE-3	67.94	0.26	11.20	12.21	0.02	0.24	0.76	6.38	0.07	0.09	0.00	99.17
CVE-4	4.95	0.70	0.49	86.97	0.07	0.23	2.65	0.29	0.07	2.90	0.00	99.32
CV-7	65.93	0.47	14.40	8.68	0.02	0.08	0.56	9.03	0.20	0.09	0.00	99.46

Geochronology. The location of the samples used for geochronology are shown in Figure 4. Scanning electron microscope photographs of representative zircons and corresponding analyses are shown in Figure 6. The U-Pb zircon geochronology results are summarized in Figure 7 while REE concentrations are summarized in Figure 8 and Table 2. Supplemental Files S1–S6 provide all data collected for each of the geochronology samples.

Any study of U-Pb zircon systematics in high-grade terranes should be approached with caution due to well-documented issues of Pb-loss, resetting/recrystallization, inheritance, and the limitations (spot size, depth, precision, etc.) of the various techniques employed. This is particularly true in the study area where ore bodies occur along faults and hydrothermal/metasomatic alteration is anticipated or, in this case, demonstrated previously [12,13,16,36,42]. We utilized optical, CL, and BSE examination and zircon REE concentrations, in concert with field observations, to evaluate the U-Pb results. None of the samples investigated show evidence of high-grade metamorphic mineral assemblages. However, it is likely that the rocks interacted with metasomatic fluids capable of chemical and isotopic changes. Recrystallization, resetting, growth, and several generations of apatite, monazite, and other U-Th trace minerals have been documented previously in the ores e.g., [44,45]. In some samples from the mining district, small fractures and areas of alteration contain secondary minerals (chlorite, actinolite, hematite, calcite, etc.) thought to be associated with lower-temperature events, which occurred as much as 60 million years after intrusion [44].

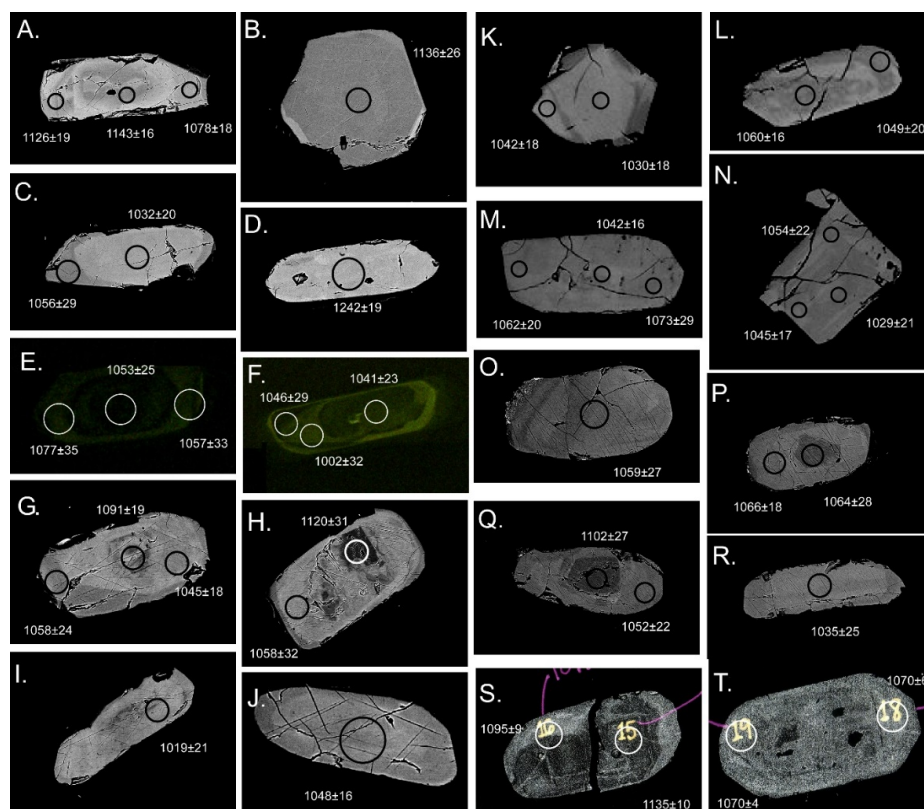


Figure 6. Backscatter electron (BSE) or cathodoluminescence (CL) mode scanning electron photomicrographs of representative zircon grains and analyses from each sample. The circles in each photograph are 30 μm and represent laser ablation analysis locations. $^{207}\text{Pb}/^{206}\text{Pb}$ ages given. (A) CVE-1 BSE. Subhedral, elongate grain with irregularly zoned core (1143 ± 16 Ma), oscillatory zoning (1126 ± 19 Ma), homogeneous rim (1078 ± 18 Ma), and euhedral inclusion (dark). (B) CVE-1 BSE. Subhedral, equant grain with homogenous core (1145 ± 17 Ma) and thin ($<10 \mu\text{m}$) rim (undated). (C) CVE-1 BSE. Dipyrarnidal grain with bright core (1032 ± 20 Ma) and darker edge of grain (1056 ± 20 Ma). (D) CVE-1 BSE. Euhedral elongate dipyrarnidal grain with a homogenous interior (1242 ± 19 Ma), which was interpreted as a xenocryst. (E) CVE-2 CL. Euhedral, elongate dipyrarnidal crystal with dark, zoned center (1053 ± 25 Ma) and lighter concentric rim (1057 ± 33 and 1077 ± 35 Ma). (F) CVE-2 CL. Euhedral, elongate dipyrarnidal crystal with dark, unzoned center (1041 ± 23 Ma) and lighter zoned concentric rims (1046 ± 23 and 1046 ± 29 Ma). (G) CVE-3 BSE. Subhedral, elongate, dipyrarnidal crystal with mottled core (1091 ± 19 Ma), light inner rim (1045 ± 18 Ma), and dark outer rim (1058 ± 24 Ma). (H) CVE-3 BSE. Rectangular grain with a complex, mottled core (1120 ± 31 Ma) and lighter rim (1058 ± 24 Ma). (I) CVE-3 BSE. Subhedral, elongate dipyrarnidal grain with a mottled core (undated) and brighter, homogenous rim (1019 ± 21 Ma). (J) CVE-3 BSE. Subhedral, elongate dipyrarnidal, homogenous grain with vague internal zonation (1048 ± 16 Ma). (K) CVE-4 BSE. Equant, anhedral crystal with homogenous center (1030 ± 18 Ma) and edge (1042 ± 18 Ma). (L) CVE-4 BSE. Elongate, dipyrarnidal grain with a mottled center (1049 ± 20 Ma) and a homogeneous edge (1060 ± 16 Ma). (M) CVE-4 BSE. Elongate, dipyrarnidal, homogeneous grain with tiny, black quartz inclusions (center— 1042 ± 16 Ma, edge— 1060 ± 20 Ma). (N) CVE-4 BSE. Rectangular, concentrically zoned, grain (center— 1029 ± 21 Ma, edges— 1045 ± 17 and 1054 ± 22 Ma). (O) CV-7 BSE. Slightly rounded, elongate, subhedral grain with zoning (1059 ± 27 Ma). (P) CV-7 BSE. Slightly rounded, elongate, subhedral grain with dark, homogenous interior (1064 ± 28 Ma) and brighter, homogenous outer zone (1066 ± 18 Ma). (Q) CV-7 BSE. Slightly rounded, elongate, subhedral grain with a dark core (1102 ± 27 Ma) and zoned rim (1052 ± 22 Ma). (R) CV-7 BSE. Slightly rounded, elongate, subhedral grain with a homogeneous core (1035 ± 25 Ma). (S) CV-2013. Slightly elongate, dipyrarnidal grain with dark resorbed and zoned core (1135 ± 10 Ma) and bright, discontinuous rim (1095 ± 9 Ma). (T) CV-2013. Slightly elongate, dipyrarnidal grain with a mottled, inclusion-filled core (undated) and oscillatory zoned rim (1070 ± 4 and 1070 ± 6 Ma).

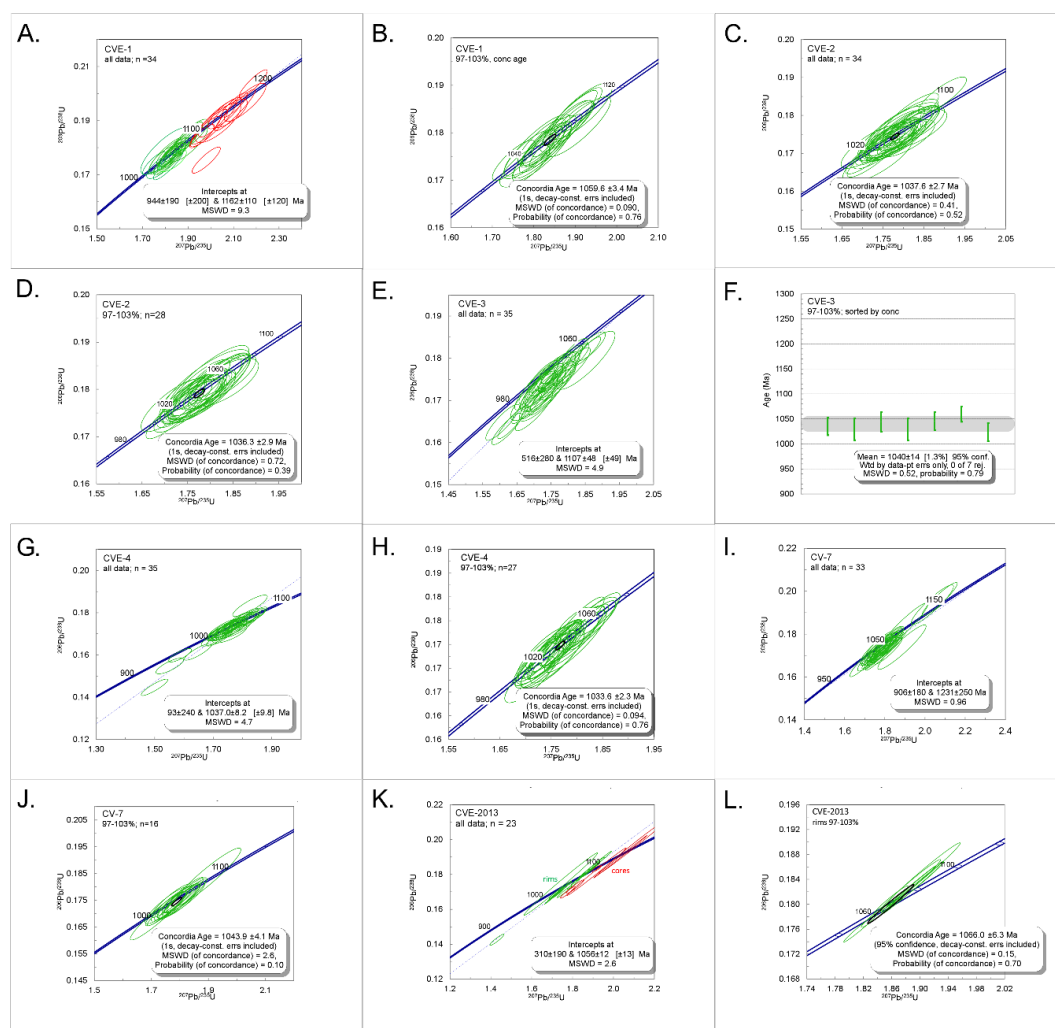


Figure 7. Weighted average and concordia diagrams for the samples analyzed in this study. (A&B) CVE-1, (C&D) CVE-2, (E&F) CVE-3, (G&H) CVE-4, (I&J) CV-7, and (K&L) CV-2013.

Table 2. U-Pb zircon geochronological results from ore and altered host rock, Cheever Mine, NY.

Sample Lat./Long. in DD	Lithology Dominant Minerals	Number Population ¹	Age (Ma) ²	U (ppm)	U/Th Ratio
CVE-1	Leucogranite	21 rims	1059.6 ± 3.4 CA	1149 ± 837	10.1 ± 7.9
44.0814-73.4528	Plg-Qtz-Mag	13 cores	Cores 1103-1242	976 ± 696	9.3 ± 11.0
CVE-2	Leucogranite	34/35	1036.3 ± 2.9 CA	188 ± 90	4.0 ± 1.0
44.0814-73.4528	Plg-Qtz-Per-Mag	homogeneous	1040 ± 11 WA	1740 ± 294	11.2 ± 5.6
CVE-3	Leucogranite	35/35	1040 ± 11 WA	1740 ± 294	11.2 ± 5.6
44.0814-73.4528	Plg-Qtz-Cpx-Mag	homogeneous	1033.6 ± 2.9 CA	986 ± 310	6.8 ± 4.5
CVE-4	Ore	27/35	1033.6 ± 2.9 CA	986 ± 310	6.8 ± 4.5
44.0814-73.4528	Mag-Ap-Cpx-Qtz	homogeneous	1033.6 ± 2.9 CA	986 ± 310	6.8 ± 4.5
CV-7 44.0776-73.4506	Leucogranite	33/35	1043.9 ± 4.1 CA	665 ± 271	5.8 ± 2.0
	Plg-Qtz-Mag	homogeneous	1043.9 ± 4.1 CA	665 ± 271	5.8 ± 2.0
CV-2013	Leucogranite	17 rims 6	1066.0 ± 6.3 CA	1326 ± 234	6.4 ± 2.1
44.0802-73.4532	Plg-Qtz-Mag-Cpx	cores	Cores 1091-1136	1107 ± 474	2.6 ± 1.4

¹ Homogeneous zircon populations are considered to reflect a single crystallization event. ² Regression technique: CA: concordia age, WA: weighted average.

Our approach to interpreting the geochronological results presented in this study is outlined in detail below. While four of the six samples have a single, well-defined population of igneous zircons, two are clearly more complicated. Typical complications include Pb-loss especially in zircons with elevated U concentrations, older ²⁰⁷Pb/²⁰⁶Pb ages, and visible core/rim relations. In this discussion,

“rim” and “core” designations are used when optically distinct interior and exterior areas are seen within individual zircon crystals and were verified by targeted spot analyses on the same grain cross-section. Inner versus outer and/or the center versus the edge is used when no significant age differences could be verified within an individual grain with multiple analyses. Such grains are considered “homogeneous” with regards to their U-Pb systematics in the cross-section analyzed and at the scale of the ablation pit.

For each sample, the data was regressed and analyzed in several ways [46]. These included standard Concordia diagrams displaying all the data collected, weighted average diagrams with data arranged by increasing $^{207}\text{Pb}/^{206}\text{Pb}$ age, and by increasing concordancy, a weighted average diagram utilizing only those analyses that fall between 97% to 103% concordant and a Concordia age diagram. In addition, individual spots analyzed were plotted on scatter plots showing U/Th versus concordancy, U versus concordancy, U versus U/Th, and concordancy versus $^{207}\text{Pb}/^{206}\text{Pb}$. Ablation pits for zircon REE analyses were located directly adjacent to ablation pits used for U-Pb analyses. This approach allowed screening for Pb-loss, alteration, inheritance, concordancy, and homogeneity of the zircon population.

Geochronological constraints suggest that the interval between crystallization of the leucogranite and its alteration is limited, which complicates the interpretation of Pb-loss trajectories that would parallel the Concordia curve [35]. When they exist, both cores (red) and rims (green) are shown on the plots. To save space, only the Concordia (all data) and final age diagrams (Weighted Average or Concordia Age) are shown in the manuscript. All weighted average diagrams are displayed at the same scale to allow for direct comparison between samples (Figure 7).

CVE-1. Sample CVE-1 is a magnetite-rich, altered leucogranite composed of albite, quartz, and magnetite. Trace minerals include zircon and monazite. It is exposed on the face of the quarry where it occurs as a 3-meter thick sheet cut by the ore and in contact with overlying sample CVE-2 and an undated gabbro body. It contains 70.59% SiO_2 , 10.68% FeO_T , 5.77% Na_2O , 0.64% K_2O , and 0.36% CaO (all in wt. %).

While variable in detail, most zircons from sample CVE-1 are elongated (4:1), have an average length of 300 μm , and have core-rim relations (Figure 6A–D). The external shape of the zircon ranges from subhedral to slightly rounded or equant. Although quite variable, cores and rims are both enriched in uranium (ca. 1000 ppm) and have U/Th ratios averaging ca. 10. Cores appear slightly brighter but patchy in BSE. The rims are slightly darker and more homogeneous in appearance. Zoning and inclusions are more prevalent in core regions.

Thirty-four of 35 analyses passed initial quality screening and 28/34 are 97% to 103% concordant. The analyses are distributed along Concordia between ca. 1030 and 1170 Ma (Figure 7A). When analyses are separated by their position as “cores” or “rims,” they yield two clusters with the rims centered on 1060 Ma and cores and/or xenocrysts with $^{207}\text{Pb}/^{206}\text{Pb}$ ages up to 1242 ± 19 Ma (Figure 6D). A weighted average diagram for all analyses yields an age of 1091 ± 15 (MSWD = 3.4). A weighted average diagram for all rims analyses that are 97% to 103% concordant yields an age of 1062 ± 10 (MSWD = 0.66). A Concordia age from the same subset of zircons is 1059.6 ± 3.4 Ma (MSWD = 0.09, Figure 7B).

Interpretation. The physical, chemical, and isotopic characteristics of zircons from sample CVE-1 display considerable variability. This variability is likely the result of the incorporation of inherited zircon from the source rock(s). Most, but not all, of the inherited zircon is incorporated into the center of large igneous grains mantled by thick rims while some remain as discrete xenocrysts. The outer portion of many grains (rims) and homogeneous grains, which lack cores, yield an age of 1059.6 ± 3.4 Ma. This is interpreted as the time of crystallization.

CVE-2. Sample CVE-2 is an altered leucogranite composed of albite, quartz, perthite, and magnetite. Trace minerals include zircon, monazite, and titanite. A sharp boundary between a magnetite-rich and magnetite-lean layers, which is apparent in the thin-section, is thought to represent compositional layering. CVE-2 is exposed on the face of the quarry where it occurs as the uppermost

sheet in the hanging wall in contact with sample CVE-1. It contains 80.28% SiO₂, 1.41% FeO_T, 4.80% Na₂O, 1.40% K₂O, and 0.57% CaO (all in wt. %).

The zircons separated from sample CVE-1 are elongated (4:1), have an average long dimension of 300 μm, and show distinct zoning (Figure 6E,F). The external shape of the zircon is predominantly euhedral to subhedral. A few small, bright cores are observed in CL, but most grains lack them. In general, interior portions of the zircons are darker than the outermost zones even though variation in lighter and darker zones can be seen on the small-scale. Analyses show consistent U-contents (ca. 190 ppm) and U/Th ratio of ca. 4.0.

Thirty-four of 35 analyses passed initial screening and 28/34 are 97% to 103% concordant. The analyses fall in a tight cluster along Concordia at ca. 1040 Ma (Figure 7C). A weighted average calculated from all data yields an age of 1041.0 ± 9.5 (MSWD = 0.34). A weighted average for all analyses that are 97% to 103% yields an age of 1041 ± 11 (MSWD = 0.32). A Concordia age from the same subset of zircons is 1036.3 ± 2.9 Ma (MSWD = 0.72, Figure 7D).

Interpretation. This sample is high in silica but otherwise appears to be one of the least altered by Na-metasomatism based on K₂O wt. %. The physical, chemical, and isotopic characteristics of zircons from sample CVE-2 display high similarity and suggest a single, homogeneous population of zircon. The analyses lie along Concordia and form a tight cluster at ca. 1040 Ma. The Concordia age of the zircons yield an age of 1036.3 ± 2.9 Ma, which is interpreted as the time of crystallization of the rock.

CVE-3. Sample CVE-3 is a magnetite-rich, altered leucogranite composed of albite, quartz, clinopyroxene, and magnetite. Trace minerals include monazite, apatite, and zircon. It is exposed on the face of the quarry where it occurs as the lowermost unit in contact with the overlying ore (sample CVE-4). It contains 67.94% SiO₂, 12.21% FeO_T, 6.38% Na₂O, 0.07% K₂O, and 0.76% CaO (all in wt. %).

The zircons from sample CVE-3 are homogeneous, elongated (4:1), and have an average long dimension of 300 μm. The external shape of the zircon is euhedral and dipyrmidal (Figure 6G–J). Zircons have relatively high uranium (ca. 1740 pm) concentrations and U/Th ratios of ca. 11.0. Interior regions, some of which contain cores, are generally darker and complex in BSE with brighter outer portions. Some grains show subtle zoning. Interior portions of the grains are often mottled, inclusion-rich, and have rounded to irregular shapes.

Thirty-five of 35 analyses passed initial screening and 7/35 are 97% to 103% concordant. The analyses fall in a loose cluster just below Concordia at ca. 1030 Ma (Figure 7E). A few analyses have slightly older ²⁰⁷Pb/²⁰⁶Pb ages, which are suggestive of inheritance. The weighted average calculated for all the analyses is 1062.1 ± 8.3 Ma (MSWD = 1.5). A weighted average diagram for all zircons between 97% to 103% concordant yields an age of 1040 ± 14 (MSWD = 0.52, Figure 7F). A Concordia age from the same subset of zircons is 1028.3 ± 4.3 Ma (MSWD = 3.5).

Interpretation. The physical, chemical, and isotopic characteristics of zircons from sample CVE-3 are homogeneous and suggests that the bulk of the zircon population likely formed during a single event. However, the analyses cluster loosely below Concordia. The high U-content likely resulted in Pb-loss, which increases the scatter and complicates interpretation. Inheritance was minimal. The oldest analysis gave a ²⁰⁷Pb/²⁰⁶Pb age of 1120.1 ± 31.7 Ma. The Concordia age of 1028.3 ± 4.3 Ma has a large MSWD (3.5) and the analyses fall below Concordia. The best age for the crystallization of the rock is 1040 ± 14 Ma derived from the weighted average.

CVE-4. Sample CVE-4 is a sample of the ore composed of magnetite with <15% by volume apatite, quartz, and clinopyroxene. Trace minerals include monazite and zircon. It is exposed on the face of the quarry where it occurs as a ca. 0.5 m thick sheet that cuts or is in fault contact with CVE-1 (hanging wall) and CVE-3 (foot wall). It contains 4.95% SiO₂, 86.97% FeO_T, 0.29% Na₂O, 0.07% K₂O, 2.65% CaO, and 2.90% P₂O₅ (all in wt. %).

A small number of zircons were recovered from sample CVE-4. While variable in detail, most zircons from sample CVE-4 are elongated (3:1) in shape, have an average long dimension of 400 μm, and show several very small and distinct cores (Figure 6K–N). The external shape of the zircon ranges from subhedral to euhedral. Although quite variable, zircons are enriched in uranium (ca. 1000 pm)

and have U/Th ratios of ca. 7. Zircons show slight variation in the BSE response, which is often patchy in appearance and subtle, generally wide, zonation.

Thirty-four of 35 analyses passed initial screening and 27/35 are 97% to 103% concordant. Concordant analyses cluster at ca. 1040 Ma with several discordant analyses falling off Concordia (Figure 7G). The weighted average calculated for all analyses is 1035.6 ± 6.9 (MSWD = 1.14). The weighted average for all the analyses that are 97% to 103% concordant is 1035.2 ± 6.9 (MSWD = 0.72). A Concordia age from the same subset of analyses is 1036.6 ± 2.3 Ma (MSWD = 0.09, Figure 7H).

Interpretation. The physical, chemical, and isotopic characteristics of zircons from sample CVE-4 are compatible with an igneous origin. A few, small internal areas, which are bright in BSE mode, are likely cores but were not targeted during analysis. The analyses lie along Concordia and form a cluster with some spread near 1040 Ma. The Concordia age 1036.6 ± 2.3 Ma is interpreted as the time of intrusion and crystallization of the ore.

CV-7. Sample CV-7 is a magnetite-rich, altered leucogranite composed of albite, quartz, and magnetite. Trace minerals include zircon, monazite, and apatite. It is one of numerous sheets intruding and interfingering with a large gabbroic body in the footwall of the mine. It contains 65.93% SiO₂, 8.68% FeO_T, 9.03% Na₂O, 0.20% K₂O, and 0.56% CaO (all in wt. %).

Zircons from sample CV-7 are elongated (3:1), have an average length of 450 μm, and are very similar in appearance (Figure 6O–R). Dark metamict cores are observed in a subset of grains. The external shape of the zircon ranges from subhedral to euhedral. Although variable, zircons are moderately enriched in uranium (ca. 665 ppm) and have intermediate U/Th ratios (ca. 6). Most grains lack cores and show fine to diffuse zoning. Metamictization and inclusions are prevalent in core regions.

Thirty-three of 35 analyses passed the initial screening and 16/34 are 97% to 103% concordant. The bulk of the analyses fall in a tight cluster just below Concordia at ca. 1050 Ma (Figure 7I). A weighted average calculated for all analyses is 1068.8 ± 8.5 Ma (MSWD = 1.4). A weighted average calculation for all analyses that are 97% to 103% yields an age of 1051 ± 10 (MSWD = 0.38). A Concordia age from the same subset of zircons is 1043.9 ± 4.1 Ma (MSWD = 2.6, Figure 7J).

Interpretation. The physical, chemical, and isotopic characteristics of zircons from sample CVE-7 are homogeneous. The analyses lie below Concordia in a tight cluster with a few grain interiors yielding older ages (oldest 1162.4 ± 29.5 Ma), which is presumably the core material. The outer portion of many grains and some grains lacking cores yield a Concordia age of 1043.9 ± 4.1 Ma, which is interpreted as the time of crystallization of the leucogranite.

CV-2013. Sample CV-2013 is an altered leucogranite composed of albite, quartz, clinopyroxene, and magnetite. Trace minerals include zircon and monazite. In contrast to the other granitic samples, it has a greenish color. It is exposed about 100 m south of the face of the quarry where it is crosscut by the ore (Figure 5B).

Zircons from sample CV-2013 are elongated (4:1), have an average length of 400 μm, and show well-defined core-rim relations (Figure 6S,T). The external shape of the zircon ranges from subhedral to euhedral. Cores, which dominate the interior of the zircon grains, are rounded, highly metamict, and mottled with numerous inclusions and appear resorbed. Rims are much more homogeneous in appearance, display zoning, and vary in thickness. Some grains have full rims and others are partially overgrown with rim material. Cores and rims are enriched in uranium (1326 to 1107 ppm).

Twenty-three of 25 analyses passed initial screening and 13/23 are 97% to 103% concordant. When analyses are separated by their position within the crystal, they yield two linear groups on the Concordia diagram, which shows a considerable scatter (Figure 7K). The weighted average age calculated from all rim analyses is 1060.3 ± 6.3 (MSWD = 9.2). A weighted average for all rims that are 97% to 103% concordant yields an age of 1063.5 ± 6.5 (MSWD = 6.0). A Concordia age from the same subset of zircons is 1059.6 ± 3.4 Ma (MSWD = 0.09, Figure 7L).

Interpretation. The physical, chemical, and isotopic characteristics of zircons from sample CV-2013 display considerable variability between interiors and rims. This variability results from

the incorporation of considerable amounts of inherited zircon in the magmatic precursor to this rock. Most, but not all, of the inherited zircon was incorporated into the center of large grains partially mantled by rims of variable thickness. Rims display zoning and appear to overgrow partially resorbed cores. The Concordia age of zircon rims, 1059.6 ± 3.4 Ma, is interpreted as the time of crystallization of the leucogranite.

Rare Earth Elements. The results for zircon REE analysis are shown in Figure 8 and Table 3. The REE from each analysis are plotted normalized to chondritic values [47] for comparison purposes. Aside from a few analyses of the lighter REEs in certain samples, all the REEs are found at concentrations exceeding detection limits. In general, patterns are similar with large positive cerium and negative europium anomalies and an upward arching increase from Gd to Lu ranging from 10 to 10,000 \times chondritic values. A few samples show strong enrichment in the lighter rare earth elements and these are generally samples with high U (>1000 ppm) content in zircon. Only slight differences between rims and cores in individual zircon populations are observed. The grey field on Figure 8 shows the values for zircons from albitites from the Big Sky Orogen [48].

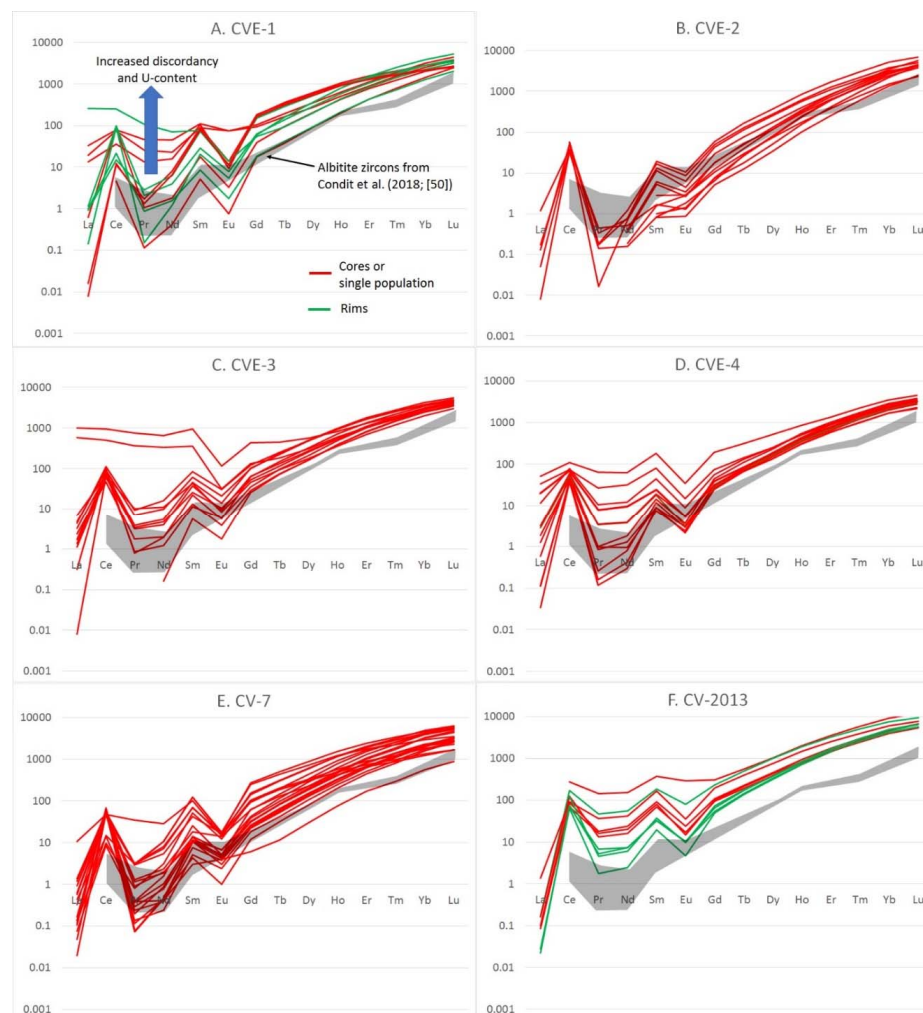


Figure 8. Chondrite-normalized rare earth element diagrams for the samples analyzed in this study. (A) CVE-1, (B) CVE-2, (C) CVE-3, (D) CVE-4, (E) CV-7, and (F) CV-2013. Thick black line shows average values from Table 3. Red lines indicate analyses from the center of homogeneous grain populations or older populations of grains interpreted as xenocrysts. The green lines are from rims when cores and rims could be readily distinguished. Grey shading represents zircons from albitites from the Big Sky Orogen (Condit et al., 2018 [48]).

Table 3. Average rare earth element concentrations measured in zircon from rock samples of the Cheever Mine, New York. Concentrations are normalized to chondritic values [47].

	La	Ce	Pr	Nd	Sm	Eu	Gd	Tb	Dy	Ho	Er	Tm	Yb	Lu
CVE-1	27.6	65.1	17.0	15.3	58.5	18.9	94.5	185.4	343	637	1064	1632	2457	3317
CVE-2	0.1	40.6	0.1	0.4	6.7	3.9	22.2	61.5	147	359	785	1521	2880	4349
CVE-3	135.8	187.3	96.9	87.2	137.2	21.6	101.0	173.8	328	640	1189	1941	3071	4251
CVE-4	10.4	59.0	9.9	10.7	35.9	7.4	50.6	106.9	210	447	816	1410	2338	3179
CV-7	0.9	44.9	2.8	4.3	36.0	8.7	75.2	155.8	307	610	1083	1692	2715	3708
CV-2013	0.2	114.4	29.0	33.4	108.6	49.9	126.7	268.5	544	1104	2027	3364	5385	7229

Interpretation. The REE patterns and concentrations for individual zircon populations show considerable variability. In zircon with “rim” and “core” targets, patterns are overlapping (CVE-1) or very similar but have differing concentrations (CV-2013). Among the samples analyzed, that of the ore (CVE-4) shows a large range in concentration but nearly identical patterns. Larger concentrations of LREE are seen in discordant zircons and strong correlations exist between U content and REE concentrations of the spot analyses in the ore zircons. Taken together, these characteristics are compatible with an igneous origin that may be slightly modified by metamictization or metasomatic processes.

5. Discussion

Zircon Characteristics. Zircons grow in a variety of metamorphic, hydrothermal, and igneous environments and often retain characteristics indicative of the conditions under which they formed. While not always unequivocal, zircon shape, size, internal structure, trace element composition, and included minerals can be used to assess their origin [48–51]. Zircon grown during hydrothermal or metasomatic events can have features like those of igneous origin [12,48–51]. However, unless the original zircons in the altered rock are completely replaced, isotopic and optical evidence of the chronology of growth should be retained. Albitites associated with the Big Sky Orogeny show zircon dissolution and precipitation associated with albitization occurring nearly 1.5 billion years after crystallization of the granodioritic host rock [48]. Rare earth element analyses, isotopic ages, shape, size, relative position, and variation in internal zonation were all used to differentiate between original zircons and metasomatic zircons. Of interest are the glomerocrystic zircon clusters noted during the in-situ analyses of the albitized rock [48].

Zircons from albitites associated with a Moroccan gold deposit are generally small (<50 μm) with solid and fluid inclusion-rich zones and have dissolution-reprecipitation textures and xenotime inclusions or overgrowths [50]. In addition, they have subdued Ce and Eu anomalies when compared to magmatic zircons. Separation of hydrothermal and magmatic zircons has been proposed using REE scatter plots [51]. In this study, REE patterns are most similar to those shown for magmatic zircons in other studies [48–51]. On scatter plots (La versus $(\text{Sm}/\text{La})_{\text{N}}$ and $(\text{Sm}/\text{La})_{\text{N}}$ versus Ce/Ce^*) zircon populations studied here plot in linear arrays below the magmatic, and to the left of the hydrothermal, fields [51].

The physical characteristics of zircon in all the samples analyzed in this study are compatible with an igneous origin (Figure 6). Their size (avg. 300 μm length), shape (dipyramidal, sub- to euhedral), and U-Pb systematics strongly support an igneous origin. Inclusions, metamict cores, core-rim relations, REE patterns, and zoning are also supportive. Several samples show clear evidence of inherited zircon cores and/or xenocrysts upon which younger zircon crystallized. The amount of inherited zircon varies widely between samples from nearly none in the sample CVE-4 from the ore and CVE-2 from a leucogranite, to thin and sometimes discontinuous rims with large cores in samples CV-2013 and CVE-1. Both core-rich samples yielded ages significantly older than the samples, which have few to no inherited zircon. These older ages may reflect the characteristics of early magmatism or, in part, arise from internal complexities in the zircon grains when targeting seemingly homogeneous areas (i.e., cores or rims).

Figure 9 shows is a plot of concordancy versus $^{207}\text{Pb}/^{206}\text{Pb}$ age for each of the zircon samples analyzed. There is a negative correlation between concordancy versus $^{207}\text{Pb}/^{206}\text{Pb}$ age in several of the samples investigated including CVE-2, CVE-3, and CVE-7. In addition, the rims in samples CVE-1 and CV-2013 also show this pattern while the cores do not. Zircons from the ore (CVE-4) lack this pattern. While the mechanism for this is not fully known, it explains why the weighted averages based on $^{207}\text{Pb}/^{206}\text{Pb}$ ages are often slightly older than the calculated Concordia age or weighted averages based on a more restricted data set (97% to 103% concordant data). The effect is slight since the ages calculated by different methods are often, but not always, within analytical error of each other.

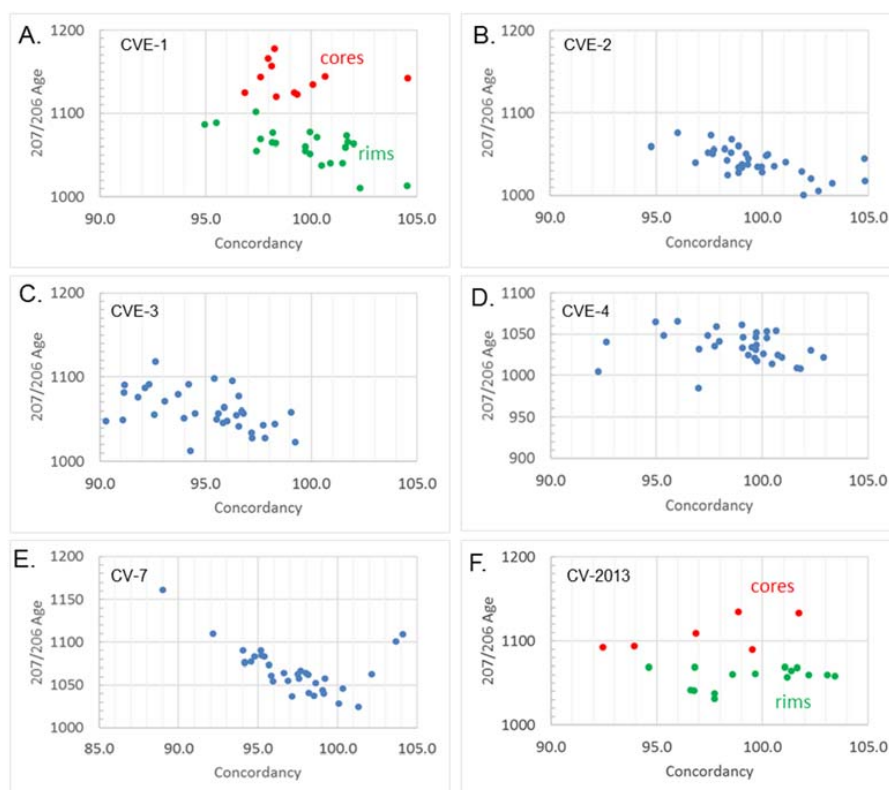


Figure 9. Scatter plots showing the variation of concordancy with the $^{207}\text{Pb}/^{206}\text{Pb}$ age for each analysis for samples: (A) CVE-1, (B) CVE-2, (C) CVE-3, (D) CVE-4, (E) CV-7, and (F) CV-2013. Blue dots represent samples with homogeneous zircon populations lacking core-rim relationships.

One possible explanation for this observation is the incorporation of inherited material in zircon ablation pit cross-sections or volumes that: (1) are either too small or indistinct to recognize optically and/or (2) sample older domains in the third-dimension. We note that zircons from the ore sample and those samples with abundant and recognizable older cores do not show the correlation between age and concordancy. The incorporation of xenocrystic zircon may be less likely in the ore due to the undersaturation of zircon in the magma at high temperatures [52]. Older cores in the altered leucogranites are often smaller, rounded, and resorbed with the apparent truncation of zoning in response to magmatic conditions.

One way to produce the negative relationship between $^{207}\text{Pb}/^{206}\text{Pb}$ and concordancy involves a two-stage Pb-loss history where relict cores or nanoscale areas of inherited Pb in zircon [53] experience Pb-loss during anatexis and incorporation in the leucogranitic magma. This initial event would facilitate migration of the U-Pb systematics on a discordia line parallel to the Concordia curve due to its nearly straight path over the relatively short interval between crystallization and anatexis (ca. 1150 to 1050 Ma). A second more recent Pb-loss event such as that related to the opening of the Atlantic or tectonic activity in the nearby Taconics/Appalachians to the east would cause discordance at the time

of disturbance (i.e., discordant array). Presumably zircon with the least amount of inherited material (or most amount of new zircon formed during the crystallization event) would be the most resistant to this second Pb-loss event due to the lack of accumulated radiation damage and, thus, remain on or near Concordia while other points become slightly discordant.

We suggest that small amounts of inherited zircon impact the U-Pb systematics observed, which results in weighted averages that give slightly older ages than those obtained from concordant analyses in the same population. These isotopically anomalous domains may be exceedingly small, optically indistinguishable, and/or intersected during ablation.

Age and origin of the iron ore. Valley et al. [12] directly dated the iron-oxide apatite ore from the Eastern Adirondacks by zircon U-Pb Secondary Ion Mass Spectrometry. Four ages were obtained ranging between 1000.9 to 1038.9 Ma and were interpreted to represent ore mineralization that was episodic and younger than the widespread and spatially associated LMG suite [12,13,16]. While the origin of the ores themselves may be in part magmatic, the physical, chemical, and isotopic properties of the zircons recovered from the ore were suggested to be compatible with a hydrothermal origin. Independent evidence for hydrothermal alteration occurs within adjacent LMG with periods of potassic and sodic alteration proposed. The later producing quartz-albite assemblages are widely associated with, and enveloping, some ore bodies [12,13,16]. The LMG host rocks analyzed from the Cheever Mine show a similar assemblage, enrichment in sodium, and, in one case, a relatively high silica content >80% by weight (Table 1), which suggests variable amounts of alteration.

Younger ages associated with late mineralization and fluids are widespread in radiogenic trace minerals within the Eastern Adirondack IOA deposits. Apatite from the IOA ore at Mineville was dated by Laser Ablation-Inductively Coupled Plasma-Mass Spectrometry yielding an age of 1009 ± 13 Ma [44]. The study of Lupulescu et al. [5] indicates numerous generations of apatite within the IOA ores with complex relationships with monazite, stillwellite-(Ce), allanite-(Ce), and thorite. Regan et al. [44] described complex symplectitic intergrowths between monazite-allanite-fluorapatite while compositionally distinct monazite not incorporated in the symplectites yielded an age of 980 ± 5.8 Ma.

These observations support the interpretation of Valley et al. [12] suggesting hydrothermal zircon in the ore samples they analyzed and brings to the forefront questions on the event(s) reflected by the ages obtained from various radiogenic minerals [44,45]. One thing that remains unknown is the extent and effects of the Rigolet pulse (980–1010 Ma) in the Adirondack region. While well documented in structures along and southwest of the Grenville Front [54], it is not yet recognized in the Adirondack Highlands or Lowlands and its effects are generally presumed, correctly or not, to be absent.

In this study, a sample of IOA ore from the Cheever Mine yields a Concordia age of 1033.6 ± 2.3 Ma by LA-MC-ICP-MS analysis of zircon U-Pb systematics. This age overlaps the age determined by Valley et al. [12] for the Palmer Hill ore body (1038.9 ± 4.4 Ma). The zircon has physical, chemical, and isotopic properties compatible with a magmatic origin. In addition, it crosscuts LMG samples within the error of the ore's age. The relationships at the Cheever Mine provide a geochronological as well as direct spatial link to the LMG. It should be noted that the LMG has been dated throughout the northern and eastern Adirondacks numerous times by a variety of techniques and the ages form a near symmetric histogram whose peak is 1047 Ma (Figure 10), which is coincident with the widespread growth of metamorphic zircon in the AH [35,36,41,55]. This suggests a significant amount of plutonism and heating occurred shortly before and/or during albitization of the leucogranitic host rocks and intrusion of the Cheever IOA ore. This time is also coincident with rapid fault movement and uplift and exhumation of the region [32–34]. Since the ore sample (CVE-4) lacks evidence for Na or K-alteration and is only slightly younger than the host rocks themselves, it places a lower limit on the timing of metasomatism (ca. 1036.6 ± 2.3 Ma) at the Cheever Mine.

As noted above, the magnetite ore at Cheever occurs as relatively thin (several meters wide), inclined, planar sheets that crosscut host rocks and can be followed along strike for as much as a kilometer or more. Where mined, the iron ore can be seen cross-cutting a variety of rock types

including granitic, intermediate, mafic meta-igneous lithologies, amphibolite, and rocks of the Grenville Supergroup. The ore is intruded by late magnetite-bearing pegmatites that have been previously dated by U-Pb zircon analyses including the Old Bed (1022.4 ± 13 Ma) and Barton Hill (1039 ± 11 Ma) mines [39]. Other late pegmatites in the region yield ages of 1025 to 1048 Ma [39] and collectively provide a minimum age range for the placement of the iron ores cut by them.

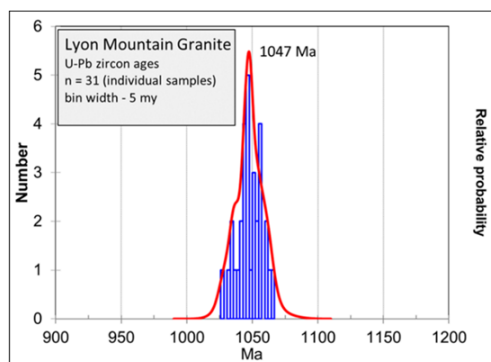


Figure 10. Histogram showing U-Pb zircon ages of Lyon Mountain Granite samples previously analyzed. Data from References [12,13,34,36,40,42].

Figure 11 shows the chronology of post-1200 Ma events in the Eastern Adirondacks and the Adirondack Highlands. While not directly dated in this study, rocks of the AMCG suite undergoing Shawinigan orogenesis, occur within a few kilometers of the Cheever Mine (Figure 3). In this study, five samples of the LMG at the Cheever Mine yield ages between 1036 to 1066 Ma in excellent agreement with the range of ages reported from elsewhere in the AH for this rock unit [40]. Although the Cheever ore does not show evidence of disturbance of the U-Pb system of zircon, monazite from the Cheever Mine has yielded ages as young as ca. 980 Ma [44]. At the Cheever Mine, we suggest that the ore is magmatic in origin, does not record the metasomatic event in the LMG host rocks it crosscuts, and younger ages from other radiogenic minerals reflect fault-related fluids and/or Rigolet metamorphic effects. Documenting the duration of ore emplacement and reconciling the information from various radiogenic minerals and documenting the timing and extent of hydrothermal alteration along with possible ore remobilization are vexing problems that remain.

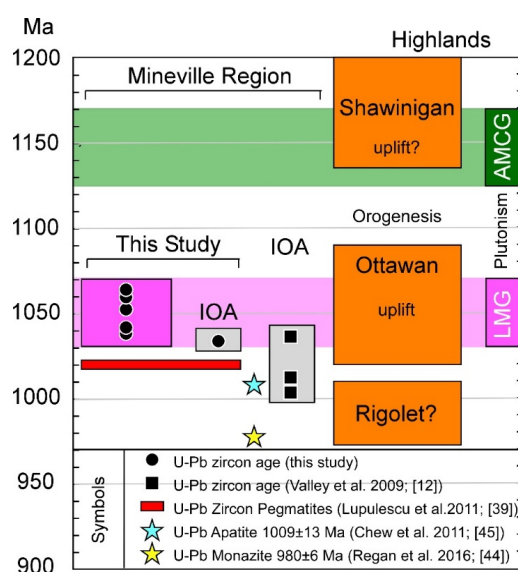


Figure 11. Summary of events recorded in the Eastern Adirondacks and regionally within the Adirondack Highlands.

6. Conclusions

The Cheever Mine in the Eastern Adirondacks of the Grenville Province provides insight into the field relations, age, and origin of the exposed IOA ore. Emplaced as an inclined, moderately west-dipping sheet, the ore cross-cuts a variety of rocks include the Lyon Mountain Granite (LMG), some gabbros/amphibolites, and metasedimentary rocks of the Grenville Supergroup.

The albite-quartz-magnetite dominated assemblages in the LMG host rocks analyzed for U-Pb zircon geochronology record variable alteration by Na-metasomatic event(s) generally restricted to the narrow-mineralized area. The ore does not show the geochemical or mineralogical traits of this alteration. The zircons associated with the ore and altered, magnetite-bearing leucogranites at the Cheever Mine, have characteristics compatible with an igneous origin. A U-Pb zircon age of ca. 1033.6 Ma determined by LA-MC-ICP-MS is interpreted at the time of intrusion of the ore.

Rocks of the LMG at the Cheever mine appear to have been emplaced as a series of concordant sheets and yield ages ranging from 1036.3–1066.0 Ma, which span the same range as has been determined from over 30 samples of the same unit throughout the eastern and northern Adirondack region. While the two oldest LMG samples at Cheever have a considerable portion of older zircon cores and xenocrysts, the younger samples generally have little or no xenocrysts documenting variable incorporation of inherited zircon, which is largely of late Shawinigan and AMCG age. The LMG samples analyzed are dominated by an albite-quartz-magnetite alteration assemblage, lack a deformation fabric and high-grade metamorphic assemblage, and show compositional banding of magnetite and layering defined by variation in grain-size, which are interpreted here as magmatic textures.

Our data suggest that, at the Cheever Mine, there is a close temporal link in addition to the well-documented spatial connection between the age of IOA ore and LMG intrusion. This suggests a genetic connection. Intrusion of LMG and its alteration was followed closely in time by intrusion of the ore utilizing the same extensional fault conduits. The field relations and age of both the IOA deposits and the LMG host further establish their post-tectonic origin related to the exhumation of the region during extensional collapse [32,33,40].

Supplementary Materials: The following are available online at <http://www.mdpi.com/2076-3263/8/9/345/s1>, Figures S1–S6.

Author Contributions: The paper was primarily written by J.R.C. with contribution and review of the co-authors. The samples were collected by M.V.L. and J.R.C. M.V.L., J.R.C., and S.P.R. analyzed the zircon samples at the Arizona Laserchron Center. J.W.S. analyzed the rare earth elements at Rensselaer Polytechnic Institute. All authors contributed to the evaluation and discussion of the data.

Funding: This research was funded by the New York State Museum and the Archie F. and Barbara Torrey MacAllaster North Country Professorship.

Acknowledgments: We thank the Real family for access to the private property where the Cheever Mine is located. This work was funded by the New York State Museum (ML) and the Archie F. and Barbara Torrey MacAllaster North Country Professorship (JC). The authors thank the Mark Pecha and staff at the Arizona Laserchron Center for their help with sample preparation and analysis. SF award NSF-EAR 1649254 to the Arizona Laserchron Center is acknowledged.

Conflicts of Interest: The authors declare no conflict of interest.

Appendix A. Analytical Procedures

Major Elements. Kilogram-size samples were pulverized using a jaw crusher and disk mill. After homogenization, a split was sent for zircon separation at the Arizona Laserchron Center and the remained pulverized in a tungsten steel ball mill. The powers set aside for major element analyses were sent to Western Washington University, made into fused disks, and analyzed by X-ray fluorescence (see web-site for technical details <https://environment.wsu.edu/facilities/geoanalytical-lab/technical-notes/>).

Geochronology. U-Pb zircon geochronology was carried out at the Arizona Laserchron Center, University of Arizona. Zircons are shown in Figure 6. U-Pb analytical results are shown in Figure 7 and in summary form in Table 2. Supplemental Files S1–S6 contain the raw data. Analyses by LA-MC-ICP-MS were conducted as previously described [56]. Ablation of zircon grains embedded in epoxy and sectioned 1/3 of the distance through was done with a Photon Machines Analyte G2 DUV193 Excimer laser using spot diameters of 30 microns with a fluence of ~ 4 J/cm² and frequency of 4 Hz. The ablated material was carried with helium-argon gas (flow rate 0.2–0.36 L/min) into the plasma source of a Nu Instruments HR ICPMS equipped with a flight tube of sufficient width that U, Th, and Pb isotopes can be measured simultaneously. All measurements were made in a static mode using Faraday detectors for ²³⁸U, ²³²Th, and ^{208–206}Pb, and discrete dynode ion-counters for ²⁰⁴Pb and ²⁰²Hg. Ion yields are typically ~ 1 mv per ppm. Each analysis consists of one 15 s integration on peaks with the laser off (for backgrounds), fifteen 1-s integrations with the laser firing, and a 30 s delay to purge the previous sample and prepare for the next analysis. The ablation pit is ~ 4 –15 microns in depth.

For each analysis, the errors in determining ²⁰⁶Pb/²³⁸U and ²⁰⁶Pb/²⁰⁴Pb result in a measurement error of $\sim 1\%$ (at 2σ level) in the ²⁰⁶Pb/²³⁸U age. The errors in measurement of ²⁰⁶Pb/²⁰⁷Pb and ²⁰⁶Pb/²⁰⁴Pb also result in $\sim 1\%$ (2σ) uncertainty in age for grains that are >1.0 Ga, but they are substantially larger for younger grains due to the low intensity of the ²⁰⁷Pb signal. For most analyses, the crossover in precision of ²⁰⁶Pb/²³⁸U and ²⁰⁶Pb/²⁰⁷Pb ages occurs at ca. 1.0 Ga. The ²⁰⁶Pb/²³⁸U ages are reported in this paper. Common Pb correction is accomplished by using the measured ²⁰⁴Pb and assuming an initial Pb composition [57] with uncertainties of 1.0 for ²⁰⁶Pb/²⁰⁴Pb and 0.3 for ²⁰⁷Pb/²⁰⁴Pb. The measurement of ²⁰⁴Pb is unaffected by the presence of ²⁰⁴Hg because backgrounds are measured on peaks (thereby subtracting any background ²⁰⁴Hg and ²⁰⁴Pb) and because very little Hg is present in the argon gas. Interelement fractionation of Pb/U is generally $\sim 20\%$ while apparent fractionation of Pb isotopes is generally $<2\%$. In-run analysis of fragments of a large zircon crystal (generally every fifth measurement through the course of analyses) with known age of 564 ± 4 Ma (2σ error) is used to correct for this fractionation. The uncertainty resulting from the calibration correction is generally $\sim 1\%$ (2σ) for both ²⁰⁶Pb/²⁰⁷Pb and ²⁰⁶Pb/²³⁸U ages. Uncertainties shown in these tables are at the 1σ level and include only measurement errors. The reported ages were calculated using Isoplot 4.0 (Figure 6) [55].

Final weighted average and concordia age diagrams (Figure 7) show two sigma uncertainties. The smaller uncertainty (labeled Mean) is based on the scatter and precision of the set of ²⁰⁶Pb/²³⁸U or ²⁰⁶Pb/²⁰⁷Pb ages, which were weighted according to their measurement errors (shown at 2σ). The larger uncertainty (final age), which is the reported uncertainty of the age, is determined as the quadratic sum of the weighted mean error plus the total systematic error for the set of analyses. The systematic error, which includes contributions from the standard calibration, age of the calibration standard, composition of common Pb, and U decay constants, is generally $\sim 1\%$ to 2% (2σ).

Analyses were conducted on zircon grains mounted in epoxy plugs and polished to yield a significant cross-section through the grain. As noted below, the grains were analyzed in a back scattered electron (BSE) and/or cathodoluminescence (CL) modes to identify internal features to be targeted or avoided (Figure 6). The sampling strategy involved analyzing 35 targeted areas selected prior to the analysis to check for variability that might arise from zoning, cores, rims, etc. Numerous grains were analyzed two or more times to check for consistency or to characterize “cores” and “rims.” Cracks, fractures, inclusions, or other heterogeneities were avoided.

Trace Elements. Trace elements in zircon were measured by LA-ICP-MS on a Photon Machines Analyte193 G1 short-pulse eximer laser coupled to Varian 820 quadrupole inductively coupled plasma mass spectrometer (Figure 8, Table 3) at RPI. All trace elements were calibrated using NIST standard glasses (#610-primary, #612 secondary). Laser parameters included 360 shots at 6 Hz repetition rate per ablation at 58% laser power attenuation and 6.5 J/cm² fluence using 20-micron square spot. Mass spectrometer acquisitions were 140 s windows each including 60 s ablation, 20 s washout, and 60 s

background acquisition. Masses analyzed by LA-ICP-MS (with millisecond dwell times in parentheses) included Ca-43 (30), Sc-45 (10), Ti-49 (1), Mn-55 (0.2), Fe-57 (1), Y-89 (10), Zr-90 (10), Sn-118 (10), La-139 (30), Ce-140 (30), Pr-141 (30), Nd-146 (30), Sm-149 (20), Eu-153 (20), Gd-157 (20), Tb-159 (20), Dy-163 (10), Ho-165 (10), Er-166 (10), Tm-169 (10), Yb-172 (10), Lu-175 (10), Hf-178 (10), W-182 (10), Pb-206 (10), Th-232 (20), and U-238 (30). The total quadrupole scan time was 465 ms per cycle, which resulted in >120 cycles within each 60-second ablation event. Each zircon sample was ablated five times in distinct locations and standards were reanalyzed every five ablations. Data was processed using the Iolite software's trace element data reduction scheme using Ti as an internal standard (as measured by EPMA).

References

- Emmons, E. Geology of New York, Comprising the Survey of the Second Geological District. In *Natural History of New York*; Mather, W.W., Ed.; Carroll and Cook: Albany, NY, USA, 1842; Volume 4.
- Jonsson, E.; Troll, V.R.; Högdahl, K.; Harris, C.; Weis, F.; Nilsson, K.P.; Skelton, A. Magmatic origin of giant 'Kiruna-type' apatite-iron-oxide ores in central Sweden. *Sci. Rep.* **2013**, *3*, 1644. [[CrossRef](#)] [[PubMed](#)]
- Maynard, G.W. The iron ores of Lake Champlain. *J. Br. Iron Steel Inst.* **1874**, *8*, 109–136.
- McKeown, F.A.; Klemic, H. *Rare-Earth-Bearing Apatite at Mineville, Essex County, New York*; U.S. Geological Survey: Reston, VA, USA, 1956.
- Lupulescu, M.V.; Hughes, J.M.; Chiarenzelli, J.R.; Bailey, D.G. Texture, Crystal structure, and composition of fluorapatites from iron oxide-apatite (IOA) deposits, eastern Adirondack Mountains, New York. *Can. Mineral.* **2017**, *755*, 399–417. [[CrossRef](#)]
- Focus Graphite and SOQUEM Announce Positive PEA for the Kwyjibo REE Project in Québec. Available online: <https://globenewswire.com/news-release/2018/06/28/1531111/0/en/Focus-Graphite-and-SOQUEM-Announce-Positive-PEA-for-the-Kwyjibo-REE-Project-in-Qu%C3%A9bec.html> (accessed on 9 September 2018).
- Bilenker, L.; Reich, M.; Simon, A.; Munizaga, R. Fe-O stable isotope pairs elucidate a high-temperature origin of Chilean iron oxide-apatite deposits. *Geochim. Cosmochim. Acta* **2016**, *77*, 94–104. [[CrossRef](#)]
- Hildebrand, R.S. Kiruna-type deposits: Their origin and relationship to intermediate subvolcanic plutons in the Great Bear magmatic zone, Northwestern Canada. *Econ. Geol.* **1986**, *81*, 640–659. [[CrossRef](#)]
- Hitzman, M.W.; Oreskes, N.; Einaudi, M.T. Geological characteristics and tectonic setting of Proterozoic iron oxide (Cu-U-Au-REE) deposits. *Precambrian Res.* **1992**, *58*, 241–287. [[CrossRef](#)]
- Corriveau, L.; Montreuil, J.-F.; Potter, E.G. Alteration facies linkages among IOCG, IOA and affiliated deposits in the Great Bear magmatic zone, Canada, in Slack, J., Corriveau, L. and Hitzman, M., eds., Proterozoic iron oxide-apatite (\pm REE) and iron oxide-copper-gold and affiliated deposits of Southeast Missouri, USA, and the Great Bear magmatic zone, Northwest Territories, Canada. *Econ. Geol.* **2016**, *111*, 2045–2072.
- Corriveau, L. *Iron-Oxide and Alkali-Calcic Alteration Ore Systems and Their Polymetallic IOA, IOCG, Skarn, Albitite-Hosted U \pm Au \pm Co, and Affiliated Deposits: A Short Course Series*; Part 1: Introduction: Geological Survey of Canada; Scientific Presentation 56; Natural Resources Canada: Ottawa, ON, Canada, 2017; p. 80.
- Valley, P.M.; Hanchar, J.M.; Whitehouse, M.J. Direct dating of Fe oxide-(Cu-Au) mineralization by U/Pb zircon geochronology. *Geology* **2009**, *37*, 223–226. [[CrossRef](#)]
- Valley, P.M.; Hanchar, J.M.; Whitehouse, M.J. New insights on the evolution of the Lyon Mountain Granite and associated Kiruna-type magnetite-apatite deposits, Adirondack Mountains, New York State. *Geosphere* **2011**, *7*, 357–389. [[CrossRef](#)]
- Westhues, A.; Hanchar, J.M.; Voisey, C.R.; Whitehouse, M.J.; Rossman, G.R.; Wirth, R. Tracing the fluid evolution of the Kiruna iron oxide apatite deposits using zircon, monazite, and whole rock trace elements and isotopic studies. *Chem. Geol.* **2017**, *466*, 303–322. [[CrossRef](#)]
- Westhues, A.; Hanchar, J.M.; LeMessurier, M.J.; Whitehouse, M.J. Evidence for hydrothermal alteration and source regions for the Kiruna iron oxide-apatite ore (northern Sweden) from zircon Hf and O isotopes. *Geology* **2017**, *45*, 571–574. [[CrossRef](#)]

16. Valley, P.M.; Fisher, C.; Hanchar, J.; Lam, R.; Tubrett, M. Hafnium isotopes in zircon: A tracer of fluid-rock interaction during magnetite–apatite (“Kiruna-type”) mineralization. *Chem. Geol.* **2010**, *275*, 208–220. [[CrossRef](#)]
17. Childress, T.; Simon, A.; Day, W.; Lundstrom, C.; Bindeman, I. Iron and Oxygen Isotope Signatures of the Pea Ridge and Pilot Knob Magnetite-Apatite Deposits, Southeast Missouri, USA. *Econ. Geol.* **2016**, *111*, 2033–2044. [[CrossRef](#)]
18. Dare, S.A.; Barnes, S.J.; Beaudoin, G. Did the massive magnetite “lava flows” of El Laco (Chile) form by magmatic or hydrothermal processes? New constraints from magnetite composition by LA-ICP-MS. *Miner. Depos.* **2015**, *50*, 607–617. [[CrossRef](#)]
19. Nyström, J.O.; Henriquez, F. Magmatic features of iron ores of the Kiruna type in Chile and Sweden; ore textures and magnetite geochemistry. *Econ. Geol.* **1994**, *89*, 820–839. [[CrossRef](#)]
20. Hofstra, A.; Meighan, C.; Song, X.; Samson, I.; Marsh, E.; Lowers, H.; Emsbo, P.; Hunt, A. Mineral thermometry and fluid inclusion studies of the Pea Ridge iron oxide-apatite-rare earth element deposit, Mesoproterozoic St. Francois Mountains Terrane, southeast Missouri, USA. *Econ. Geol.* **2016**, *111*, 1985–2016. [[CrossRef](#)]
21. Knipping, J.; Bilenker, L.; Simon, A.; Reich, M.; Barra, F.; Deditius, A.; Lundstrom, C.; Bindeman, I.; Munizaga, R. Giant Kiruna-type deposits form by efficient flotation of magmatic magnetite suspensions. *Geology* **2015**, *43*, 591–594. [[CrossRef](#)]
22. Nyström, J.O. Apatite iron ores of the Kiruna Field, northern Sweden: Magmatic textures and carbonatitic affinity. *Geologiska Föreningen i Stockholm Förhandlingar* **1985**, *107*, 133–141. [[CrossRef](#)]
23. Nyström, J.O.; Henriquez, F.; Naranjo, J.A.; Naslund, H.R. Magnetite spherules in pyroclastic iron ore at El Laco, Chile. *Am. Miner.* **2016**, *101*, 587–595. [[CrossRef](#)]
24. Rivers, T. Upper-crustal orogenic lid and mid-crustal core complexes: Signature of a collapsed orogenic plateau in the hinterland of the Grenville Province. *Can. J. Earth Sci.* **2012**, *49*, 1–42. [[CrossRef](#)]
25. Frost, C.B.; Frost, B.R. Proterozoic ferroan feldspathic magmatism. *Precambrian Res.* **2013**, *228*, 151–163. [[CrossRef](#)]
26. Roden-Tice, M.T.; Tice, S.T. Regional-scale Mid-Jurassic to Late Cretaceous unroofing from the Adirondack Mountains through central New England based on apatite fission-track and (U-Th)/He thermochronology. *J. Geol.* **2005**, *113*, 535–552. [[CrossRef](#)]
27. Lowe, D.G.; Arnott, R.W.C.; Chiarenzelli, J.R.; Rainbird, R.H. Early Paleozoic rifting and reactivation of a passive-margin rift: Insights from detrital zircon provenance signatures of the Potsdam Group, Ottawa graben. *Geol. Soc. Am. Bull.* **2018**, *130*, 1377–1396. [[CrossRef](#)]
28. Wynne-Edwards, H.R. The Grenville Province. In *Variations in Tectonic Styles in Canada*; Special Paper; Price, R.A., Douglas, R.J.W., Eds.; Geological Association of Canada: St. John’s, NL, Canada, 1972; Volume 11, pp. 263–334.
29. Moore, J.M.; Thompson, P. The Flinton Group: A late Precambrian metasedimentary succession in the Grenville Province of eastern Ontario. *Can. J. Earth Sci.* **1980**, *17*, 1685–1707. [[CrossRef](#)]
30. Rivers, T.; Martignole, J.; Gower, F.; Davidson, A. New tectonic divisions of the Grenville Province, southeast Canadian Shield. *Tectonics* **1989**, *8*, 63–84. [[CrossRef](#)]
31. Mezger, K.; van der Pluijm, B.A.; Essene, E.J.; Halliday, A.N. The Carthage-Colton Mylonite Zone (Adirondack Mountains, New York): The site of a cryptic suture in the Grenville Orogen? *J. Geol.* **1992**, *100*, 630–638. [[CrossRef](#)]
32. Bonamici, C.E.; Kozdon, R.; Ushikubo, T.; Valley, J.W. High-resolution P-T-t paths from $\delta^{18}\text{O}$ zoning in titanite: A snapshot of late-orogenic collapse in the Grenville of New York. *Geology* **2011**, *39*, 959–962. [[CrossRef](#)]
33. Selleck, B.W.; McLelland, J.; Bickford, M.E. Granite emplacement during tectonic exhumation: The Adirondack example. *Geology* **2005**, *33*, 781–784. [[CrossRef](#)]
34. McLelland, J.; Selleck, B. Megacrystic Gore Mountain-type garnets in the Adirondack Highlands: Age, origin, and tectonic implications. *Geosphere* **2011**, *7*, 1194–1208. [[CrossRef](#)]
35. Chiarenzelli, J.; McLelland, J. Granulite facies metamorphism, paleoisotherms, and disturbance of the U-Pb systematics of zircon in anorogenic plutonic rocks from the Adirondack Highlands. *J. Metamorph. Geol.* **1992**, *11*, 59–70. [[CrossRef](#)]

36. Heumann, M.J.; Bickford, M.E.; Hill, B.M.; Selleck, B.W.; Jercinovic, M.J. Timing of anatexis in metapelites from the Adirondack Lowlands and Southern Highlands: A manifestation of the Shawinigan orogeny and subsequent anorthosite-mangerite-charnockite-granite (AMCG) magmatism. *Geol. Soc. Am. Bull.* **2006**, *118*, 1283–1298. [[CrossRef](#)]
37. Chiarenzelli, J.; Valentino, D.; Lupulescu, M.; Thern, E.; Johnston, S. Differentiating Shawinigan and Ottawa orogenesis in the Central Adirondacks. *Geosphere* **2011**, *7*, 2–22. [[CrossRef](#)]
38. Chiarenzelli, J.; Kratzmann, D.; Selleck, B.; de Lorraine, W. Age and provenance of Grenville Supergroup rocks, Trans-Adirondack Basin, constrained by detrital zircons. *Geology* **2015**, *43*, 183–186. [[CrossRef](#)]
39. Lupulescu, M.; Chiarenzelli, J.; Pullen, A.; Price, J. Using pegmatite geochronology to constrain temporal events in the Adirondack Mountains. *Geosphere* **2011**, *7*, 23–39. [[CrossRef](#)]
40. Chiarenzelli, J.; Selleck, B.; Lupulescu, M.; Regan, S.; Bickford, M.E.; Valley, P.; McLelland, J. Lyon Mountain ferroan leucogranite suite: Response to collision, thickened crust, and extension in the core of the Grenville Orogen. *Geol. Soc. Am. Bull.* **2017**, *129*, 1472–1488. [[CrossRef](#)]
41. McLelland, J.; Hamilton, M.; Selleck, B.; McLelland, J.M.; Walker, D.; Orrell, S. Zircon U-Pb geochronology of the Ottawa orogeny, Adirondack Highlands, New York: Regional and tectonic implications. *Precambrian Res.* **2001**, *109*, 39–72. [[CrossRef](#)]
42. McLelland, J.; Morrison, J.; Selleck, B.; Cunningham, B.; Olson, C.; Schmidt, K. Hydrothermal alteration of late- to post-tectonic Lyon Mountain granitic gneiss, Adirondack Mountains, New York: Origin of quartz-sillimanite segregations, quartz-albite lithologies, and associated Kiruna-type low Ti-Fe-oxide deposits. *J. Metamorph. Geol.* **2002**, *20*, 175–190. [[CrossRef](#)]
43. Kemp, J.F. The Mineville-Port Henry mine group in Geology of the Adirondack magnetic iron ores, Newland, D.H., Ed. *N. Y. State Mus. Bull.* **1908**, *119*, 57–88.
44. Regan, S.; Lupulescu, M.; Jercinovic, M.; Singer, J.; Geer, P.; Chiarenzelli, J.; Williams, M.; Walsh, G. Geochronology of IOA-type deposits: What are we dating? *Geol. Soc. Am. Abstr. Programs* **2016**, *48*, 7.
45. Chew, D.; Sylvester, P.; Tubrett, M. U-Pb and Th-Pb dating of apatite by LA-ICPMS. *Chem. Geol.* **2013**, *280*, 200–216. [[CrossRef](#)]
46. Ludwig, K. *Isoplot 3.7 and 4.1*; Berkeley Geochronology Center: Berkeley, CA, USA, 2008; Available online: https://www.bgc.org/isoplot_etc/isoplot.html (accessed on 9 September 2018).
47. Sun, S.S.; McDonough, W.F. *Chemical and Isotopic Systematics of Oceanic Basalts*; Saunders, A.D., Norry, M.J., Eds.; Geological Society of London: London, UK, 1989; Volume 42, pp. 313–345.
48. Condit, C.; Mahan, K.; Curtis, K.; Moeller, A. Dating metasomatism: Monazite and zircon growth during amphibolite facies albitization. *Minerals* **2018**, *8*, 187. [[CrossRef](#)]
49. Wu, Y.; Zheng, Y. Genesis of zircon and its constraints on the interpretation of U-Pb age. *Chin. Sci. Bull.* **2004**, *49*, 1554–1569. [[CrossRef](#)]
50. Pellerer, E.; Cheilletz, A.; Gasquet, D.; Mouttaqi, A.; Annich, M.; Deloule, E. Hydrothermal zircons: A tool for ion microprobe U-Pb dating of ore mineralization in polyphase deposits. *Chem. Geol.* **2007**, *245*, 135–161. [[CrossRef](#)]
51. Fu, B.; Mernagh, T.P.; Kita, N.T.; Kemp, A.I.; Valley, J.W. Distinguishing magmatic zircon for hydrothermal zircon: A case study from the Gidindurh high-sulphidation Au-Ag-(Cu) deposit of SE Australia. *Chem. Geol.* **2009**, *259*, 131–148. [[CrossRef](#)]
52. Miller, C.F.; McDowell, S.M.; Mapes, R.W. Hot and cold granites? Implications of zircon saturation temperatures and preservation of inheritance. *Geology* **2003**, *31*, 529–532. [[CrossRef](#)]
53. Valley, J.W.; Reinhard, D.A.; Cavosie, A.J.; Ushikubo, T.; Lawrence, D.F.; Larson, D.J.; Kelly, T.F.; Snoeyenbos, D.R.; Strickland, A. Nano- and micro-geochronology in Hadean and Archean zircons by atom-probe tomography and SIMS: New tools for old minerals. *Am. Miner.* **2015**, *100*, 1355–1377. [[CrossRef](#)]
54. Hynes, A.; Rivers, T. Protracted continental collision—Evidence from the Grenville Orogen. *Can. J. Earth Sci.* **2010**, *47*, 591–620. [[CrossRef](#)]
55. McLelland, J.; Chiarenzelli, J.; Whitney, P.; Isachsen, Y. U-Pb zircon geochronology of the Adirondack Mountains and implications for their geologic evolution. *Geology* **1988**, *16*, 920–924. [[CrossRef](#)]

56. Gehrels, G.E.; Valencia, V.; Ruiz, J. Enhanced precision, accuracy, efficiency, and spatial resolution of U-Pb ages by laser ablation-multicollector inductively coupled plasma-mass spectrometry. *Geochem. Geophys.* **2008**, *9*, 1–13. [[CrossRef](#)]
57. Stacey, J.S.; Kramers, J.D. Approximation of terrestrial lead isotope evolution by a two-stage model. *Earth Planet. Sci. Lett.* **1975**, *26*, 207–221. [[CrossRef](#)]



© 2018 by the authors. Licensee MDPI, Basel, Switzerland. This article is an open access article distributed under the terms and conditions of the Creative Commons Attribution (CC BY) license (<http://creativecommons.org/licenses/by/4.0/>).